Preprint
UCRL-JC-138661

# A Large-area PSPMT Based Gamma-ray Imager with Edge Reclamation

*K.-P. Ziock, L. Nakae*

This article was submitted to
2000 Institute of Electrical and Electronics Engineers Nuclear Science Symposium and Medical Imaging Conference, Lyon, France, October 15-20, 2000

**September 21, 2000**

U.S. Department of Energy
Lawrence Livermore National Laboratory

DISCLAIMER



This work was performed under the auspices of the United States Department of Energy by the University of California, Lawrence Livermore National Laboratory under contract No. W-7405-Eng-48.

# A Large-area PSPMT Based Gamma-ray Imager with Edge Reclamation*

Klaus-Peter Ziock, Les Nakae

Lawrence Livermore National Laboratory, P.O. Box 808, Livermore, CA 94550

## *Abstract*

We describe a coded aperture, gamma-ray imager which uses a CsI(Na) scintillator coupled to an Hamamatsu R3292 position-sensitive photomultiplier tube (PSPMT) as the position-sensitive detector. We have modified the normal resistor divider readout of the PSPMT to allow use of nearly the full 10 cm diameter active area of the PSPMT with a single scintillator crystal one centimeter thick. This is a significant performance improvement over that obtained with the standard readout technique where the linearity and position resolution start to degrade at radii as small as 3.5 cm with a crystal 0.75 cm thick. This represents a recovery of over 60% of the PSPMT active area. The performance increase allows the construction of an imager with a field of view 20 resolution elements in diameter with useful quantum efficiency from 60-700 keV. In this paper we describe the readout technique, its implementation in a coded aperture imager and the performance of that imager.

## I. INTRODUCTION

Uniformly redundant array based coded aperture imaging was developed by the Astrophysical community over 30 years ago for use in gamma-ray astronomy.[1] The first terrestrial version of such an instrument, designed for use in arms control inspections, was reported fifteen years later.[2] Since that time, the utility of coded aperture imagers has been demonstrated for use as a tool for treaty inspections, transparency inspections, safeguards and environmental restoration and radioactive waste management.[3] In this paper we present the next generation of our portable Gamma-Ray Imaging Spectrometer (GRIS), which has an active area three times that of the current generation of commercial instruments[4] while also providing an improvement in high energy response over our previous imager.

## II. CODED APERTURE IMAGING

The ability to penetrate significant amounts of matter is one of the properties that makes gamma-rays a useful diagnostic when working with fissile materials. Unfortunately, this property also makes generating an image with this radiation particularly difficult. Lenses and mirrors which can be successfully applied at photon energies up to ~ 100 keV[5] are no longer effective at the energies of interest. (For our applications, the low end of the energy band is generally defined by the ~ 100 keV k-shell radiation emitted by U and can extend to several MeV.) To overcome this difficulty, we use the coded aperture imaging technique. This method relies on a mask which is half open area, to cast a shadow of a portion of its area onto a position-sensitive detector. The pattern is designed to autocorrelate to a delta function.[1] This property means that a source in any pixel in the field of view projects a unique portion of the shadow mask on to the detector. Further, the pattern generated by a source in one pixel does not generate cross-talk with that created by other pixels (other than through statistical fluctuations). The image is generated by performing a cross-correlation between the mask and the pattern recorded by the detector.

The large open area of such a system can provide a significant improvement in imaging signal to noise ratio over that of a simple pin-hole camera. In a background dominated measurement of a point source, one wins by the square root of the number of open pixels,[6] or a factor of ~ 12 for our rank-9 hex, uniformly redundant array pattern.[7]

In a coded aperture imager, the position resolution, $\Delta x$, at an object at distance, d, is given by:

$$\Delta x = d\frac{a}{f} \tag{1}$$

where a is the size of the holes in the mask and f, the focal length, is the spacing between the mask and the detector. By varying the focal length, one can give the imager a variable zoom feature.

In addition to a shadow mask, a successful imager requires a position-sensitive detector to record the shadow pattern. The properties of the detector are key to designing the overall imager. To avoid loss in detail, the detector resolution should be able to twice resolve the basic mask feature size. Detector resolution also determines the focal length required to achieve a given target resolution and hence the length of the imager. The number of resolution elements across the detector determines the mask pattern and number of pixels in the field of view. To accommodate magnification of the mask pattern at the detector from sources at finite distances, a variable pixel size makes implementing a zoom feature much easier. The energy range of the detector determines the energy range of the instrument and the mask thickness required to cover that range. The mask thickness is also limited by self collimation effects if the pixel size is very small. Finally, the energy resolution of the detector is important to generate isotope specific images and or to reduce image noise in applications with complicated spectral emissions.

* This work was performed under the auspices of the U.S. Department of Energy by Lawrence Livermore National Laboratory under Contract W-7405-Eng-48

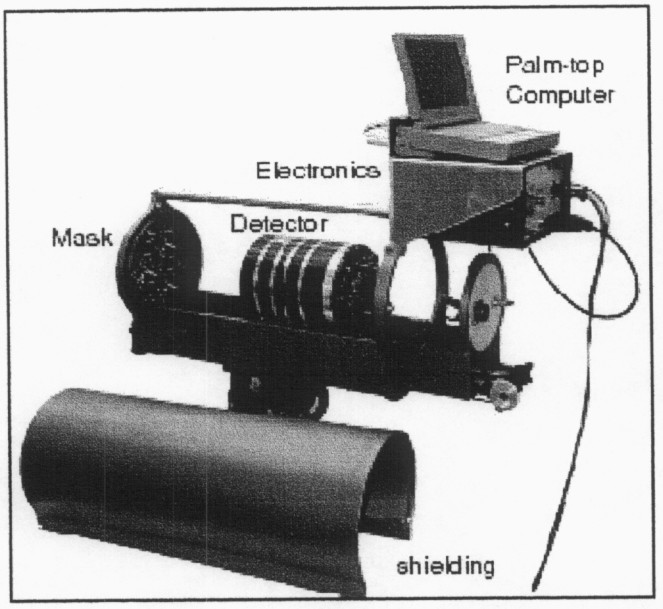


Figure 1. Complete imager with cover removed showing mask, detector and electronics. The shielding shown below the imager head slides over the detector along the system axis.

## III. INSTRUMENT DESIGN

A photograph of the imager is shown in Fig. 1. It comprises a position-sensitive detector mounted on a linear bearing; a hex, uniformly-redundant-array, coded aperture mask; shielding and the data acquisition system. The instrument can be set to any of 5 preset focal lengths providing a factor of 3.7 zoom. The mask is cut from one millimeter thick tantalum sheets, five of which are laminated to form the total 0.5 cm thickness. It is based on a rank 9 HURA (hex uniformly redundant array)[7] with a single pixel hex side length of 2.42 mm and a center-to-center spacing of 4.19 mm. Lead shielding 9.5 mm thick is permanently mounted below the linear slide. Top and side shielding is provided by a separate partial cylinder 9.5 mm thick which can be slid over the imager. The detector, is based on a Hamamatsu R3292, 10 cm diameter, active area, position-sensitive, photomultiplier tube (PSPMT)[8] coupled to a one centimeter thick CsI(Na) crystal. The acquisition system uses custom gated integrator circuits coupled into an 8 channel, 16 bit digitizer card. The instrument is controlled by a modified version of commercial software obtained from RMD Corporation.[4]

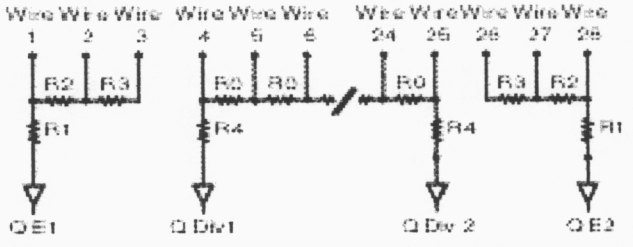


Figure 2. Schematic diagram of the modified tube readout in one dimension. Although the end wires are read from only one side, the inline resistors have been left to maintain the potential values as if a divider were present. This avoids affecting the trajectory of the electrons in flight and hence distorting the shape of the charge cloud collected.

### *1. Detector Design*

In developing this instrument, our goal was to maintain the ~ 19 x 17 resolution elements (37 x 33 pixels) of our current coded aperture imager. To obtain the requisite 36 pixels across the 10 cm diameter PSPMT, this requires a resolution of order three millimeters. In practice, the available diameter is less than 10 cm because the performance of the system degrades at the edges and because the mask pattern at the detector is magnified when acquiring images of objects at finite distances. The degree of magnification is a function of the resolution at the target and must be accounted for before the image deconvolution is undertaken.

The detector uses a Hamamatsu R3292 PSPMT photomultiplier tube coupled to a one centimeter thick, 12 cm diameter CsI(Na) crystal. The crystal (specular polish on all faces) is glued to the PSPMT face using Rexon RX 22P[9] coupling compound. Graphite blackened silicone compound is used to pot the edges of the crystal and reduce light cloud reflection and position distortion as outlined below. The top face is covered with Teflon micropore tape and a 125 $\mu$m thick aluminum window is used to hermetically seal the system. Further details on the selection and preparation of the crystal can be found in ref [10].

#### *1. On-Axis, Edge Reclamation*

A PSPMT based gamma-ray detector generates an event location via a centroiding process. The incident gamma-ray is converted to scintillation light by the crystal. Through proximity, this creates a localized "spot" of photoelectrons from the photocathode. The electron spot is amplified in a spatially coherent manner using mesh dynodes. A crossed-wire anode collects the amplified signal and feeds it into a resistor divider network (see Fig. 2) By measuring the charge, $q_i$, from each end of the divider, the location of an event in one dimension is determined through the use of the simple formula:

$$X = \frac{q_1}{q_1 + q_2} \tag{2}$$

The energy of the event is given by the sum of all four $q_i$ values (two from the divider in each dimension). This process determines the centroid of the charge (and hence light) spot location.[11] As shown in reference [10] this "spot" is actually a rather broad distribution with a Gaussian profile of order several centimeters. One obtains a position resolution of ~ 3 mm only by virtue of the large amount of scintillation light which is generated in the crystal. The centroiding process means that the position resolution scales as the square root of the gamma-ray energy.[11]

While a good position determination can be made near the center of the tube, one starts to have problems with this technique as the events approach the edge of the detector. A

simplistic explanation argues that when the light cloud strikes the edge of the crystal it will tend to bounce back toward the center. Since the center of the cloud does not move as far as it should, events near the tube edge show up in a narrow range of electronic values resulting in tube distortion and poor position resolution. Due to the several centimeter size of the light cloud, edge distortion occurs for events which are only at a radius of ~ 3 cm from the center of the tube and completely dominates events greater than 3.5 cm from the center. This significantly limits the useful area of the device.

In reference [10] we report a more detailed examination of this effect by measuring the signal from individual wires of the anode as a collimated $^{133}$Ba source was moved across the tube face. These measurements indicate that the poor resolution at the tube edge is due to a more complicated interpretation, including changes in the electron cloud amplification. A phenomenological approach allows us to devise a relatively low-cost improvement based on the observation that the end wires continue to provide useful position information although the overall divider response has fallen off. We capitalized on this by removing the last three wires at each end of the anode from the divider readout. The end wires are connected and read out with a single additional electronics channel for each side of the tube (see Fig. 2). Through this simple modification and the use of the four additional readout channels we are able to reclaim a significant fraction of the lost detector area.

*2. Position Determination*

Our previous, on-axis work used the following expression to determine an event location in each dimension:[10]

$$X = \frac{q_1}{q_1 + q_2} + 0.5\frac{\left|q_{e1}^2 - q_{e2}^2\right|}{(q_1 + q_2)^2} \qquad (3)$$

Here the e subscript refers to values from the (edge) wire only read outs. Note that the first term is the same as the simple divider expression and is valid for events near the center of the tube. The second term generates a position as determined from

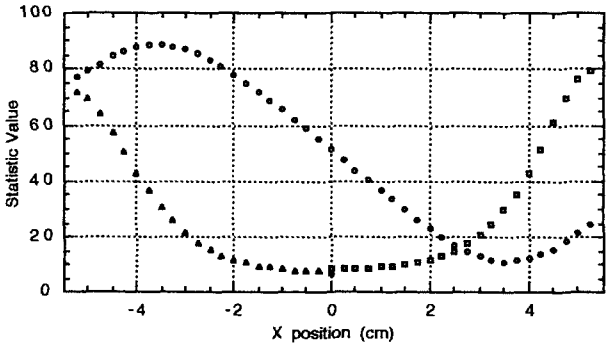


Figure 3. X Statistic values as defined in equation (4) at y=0 cm The circles represent the divider statistic, the triangles and squares represent the left and right edge statistics respectively. Note that the edge values are set to zero (not shown) if they are too small.

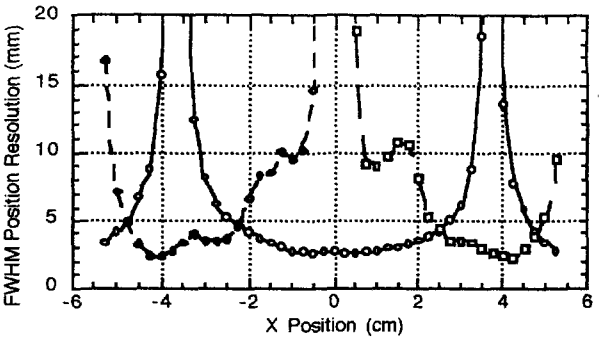


Figure 4. Derived position resolution as a function of position for y=0 scan data. The circles represent the divider statistic, the diamonds and squares represent the left and right edge statistics respectively.

the appropriate end wire and is normalized for energy as measured from the divider. The divider sum is used in the denominator because it decreases as events fall nearer the edge of the detector (see Fig. 3). This contributes to the position information at the edges. The values of the second term are squared to cause dominance at the edges where the position information is carried by the term and the 0.5 serves as an appropriate balance between the two expressions.

*3. Full-Face Edge Reclamation*

*3A. Calibration scan*

Based on the on-axis work, we completed a full, 8-channel, data acquisition system and coupled it to the detector. To determine the system performance, a calibration scan using a collimated $^{133}$Ba source (~ 1.5 mm beam diameter) was run. The source was mounted in an automated x-y translation stage and stepped across the detector face on a 2.5 mm pitch over a radius of 5.25 cm. At each location ~ 30,000 events were collected and recorded in "run-mode" data files so that they could be replayed using different event location formulas (such as equation (3).) It should be noted that, even without the 8-channel readout, such a calibration scan is required to correct for non-linearity in position and energy response from this type of detector.

*3B. Data handling*

The 1473 data files from the calibration scan were repeatedly replayed with an automated analysis routine to find the optimum technique to combine the 8 channels of data. Both position resolution and uniform quantum efficiency were used as performance criteria. The analysis routine selects events from the 356 keV energy peak at each location. For each event, an x and y position are generated and accumulated into x and y position histograms. A Gaussian function is fit to each histogram using a chi-square minimization routine,[11] and the parameters ($\chi^2$, center-location, width and respective variances) were saved to a file along with the stage locations and the peak energy channels. Different statistics and algorithms were tried to determine a data handling technique that provides the best match of histogram centroids to actual motor locations.

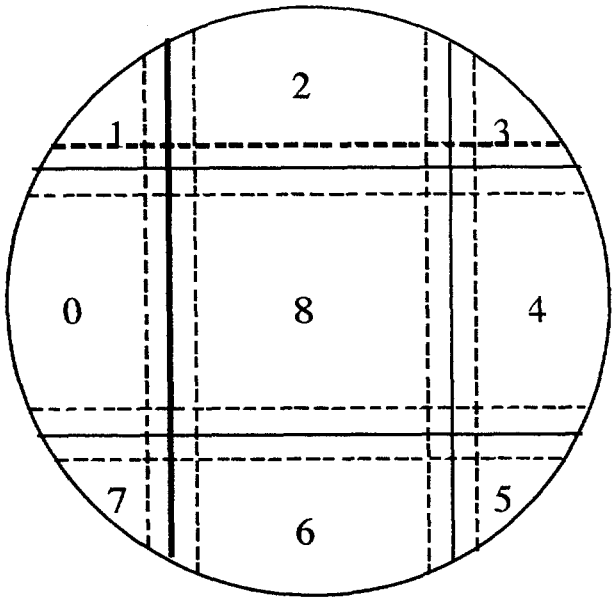


Figure 5. Tube face showing different regions. Between dotted lines more than one statistic pair can contribute to the data. The dotted line locations are at -3.0, -2.0, 2.0 and 3.0 centimeters in each dimension.

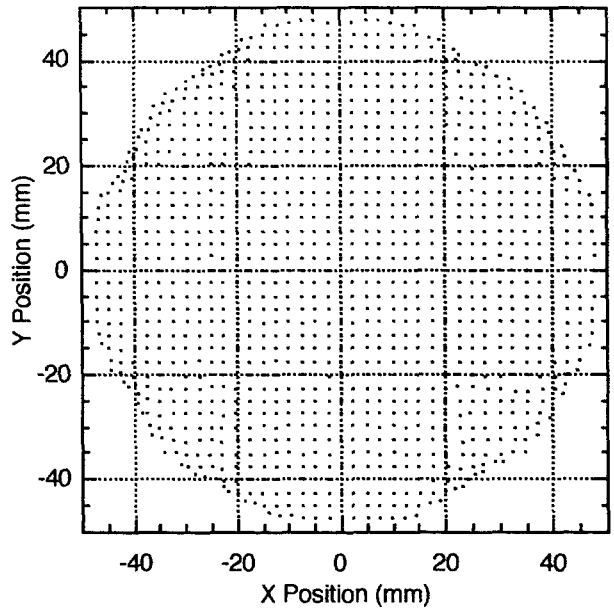


Figure 6. Fit centroids of x-y calibration scan after replay through the linearization routine.

*3C. Location Statistics*

The data linearization procedure selected relies on generating the following three position statistics in each dimension:

$$X_{e1} = \frac{q_{e1}}{q_1}; \quad X_{div} = \frac{q_1}{q_1 + q_2}; \quad X_{e2} = \frac{q_{e2}}{q_2} \qquad (4)$$

The subscripts refers to the edges (e1 and e2) and the divider (div) with the 1 and 2 referring to the signal from one side of the divider or edge. The correspondence to the on-axis equation (3) is obvious, however note that the edge statistics are now normalized only by the value from the nearest divider side. This number carries more position information than that used in equation (3).

A plot of the Gaussian center locations as a function of position in the x-direction at y = 0 cm is shown in Fig. 3. The plot clearly shows that the position information is carried by a different statistic in different areas of the tube. In particular, the divider value is multivalued, providing indeterminate event locations in some detector areas. This point is better illustrated in Fig. 4 where the y = 0 position resolution of the different statistics is plotted. This was determined by dividing the Guassian peak widths by the slope of the data in Fig. 3 (calculated from a fit of a fifth order polynomial to the data.)

*3D. Event Handling*

Due to the ambiguity in location of the general off-axis event, we are unable to use a simple expression to handle the data. Rather, the detector face is broken into 9 regions as shown in Fig. 5. With an additional four quadrants superimposed on top of this by the horizontal and vertical diameters (not shown.) An event is initially placed into quadrants based on the divider values. This is used to set the far-side edge statistics to zero, since only one edge in each dimension can carry useful information. The event is then compared with the limits of the statistics for a given region (the values were determined in the calibration process), and an event location is determined by bilinear interpolation from stored lookup tables that relate the statistic locations back to the motor locations used in the scan. The event is always treated as x,y data pairs with the border area between regions having more than one pair contributing.

The look-up tables are generated on a unity pitch for the statistic values multiplied by 100. This creates a pitch finer than the scan steps and is suitable for rapid location determination in the look-up algorithm—an important consideration for event-by-event linearization while data collection is in process.

The calibration data set is formed in an iterative fashion. Based on the original fit positions and the location algorithm outlined above, the calibration points are replayed through the linearization process and a new set of Gaussian fits performed. The centroids of these points fall on a more regular grid than the original data. However, toward the edges, distortions are still present. This indicates that the corrections are not large enough to fully shift the centroid since the scatter of points from a single measurement location will include outliers which are handled by calibration data from neighboring scan locations (and near the edge, these become progressively less reliable) To correct for this, and extend the useful range of a given statistic set, the measured centers from individual statistic pairs are artificially shifted to the far side of the true location by a value of up to 2.5 mm. The correspondence between electronic values and true positions is repeated and a

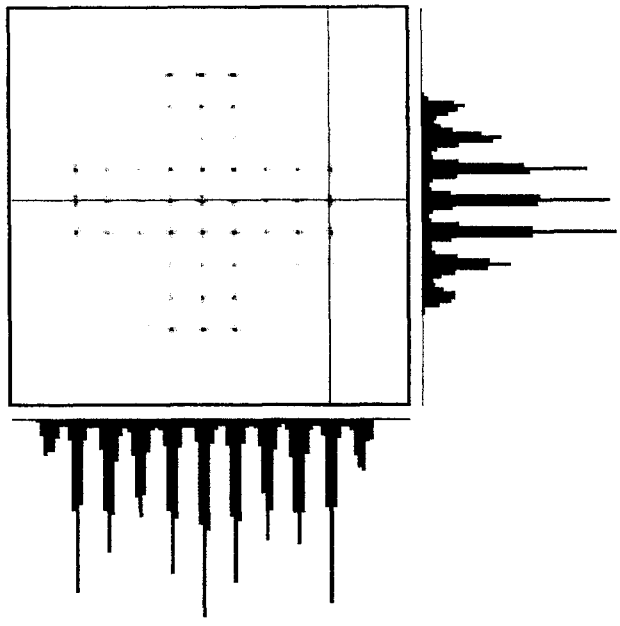

Figure 7. Grayscale image of linearized detector response to a point source scanned on a 1 cm pitch. The data along the cursors is plotted in histogram form next to the full face image. There are 8 image pixels per centimeter. Only data in the 356 keV line is included.

new calibration set is generated. When this new set is used to replay the data through the fitting routines, an improved correspondence between the adjusted centers and the original scan locations is seen (Fig. 6).

The peak energy channel from the scan data is used to make a map of the energy gain linked to the location of an event. This is used to correct the energy on an event-by-event basis once its location has been determined.

*3E. Detector performance*

The performance of the finished detector is shown in Figures 7-10. The first of these shows a grayscale image of the calibration data taken on a one centimeter pitch replayed through the linearization procedure. Figure 8 is a grayscale image of the derived position resolution as a function of position on the detector face. It was generated by replaying the calibration data through the final linearization procedure and fitting a histogram of the x and y data at each location to a Gaussian. The RMS sum of the one sigma widths of the x and y fits is plotted. The average value over the whole detector face is 2.5 mm representing a 1.8 mm value in each dimension. It is clear from the figure, that the values at the edges and particularly in the "corners" ($\pm x = \pm y$) dominate this number. For instance, the average combined RMS value over the region $35 \leq |y| \leq 20$ is 1.98 mm. Figure 9 shows the number of counts as a function of position for a full face exposure to a distant source. Ideally the detector would be uniformly gray, indicating a uniform quantum efficiency has been achieved.

The energy response of the detector is shown in Fig. 10. The top shows a whole face exposure to the $^{133}$Ba source. The bottom spectrum is the spectrum taken at a single point at the

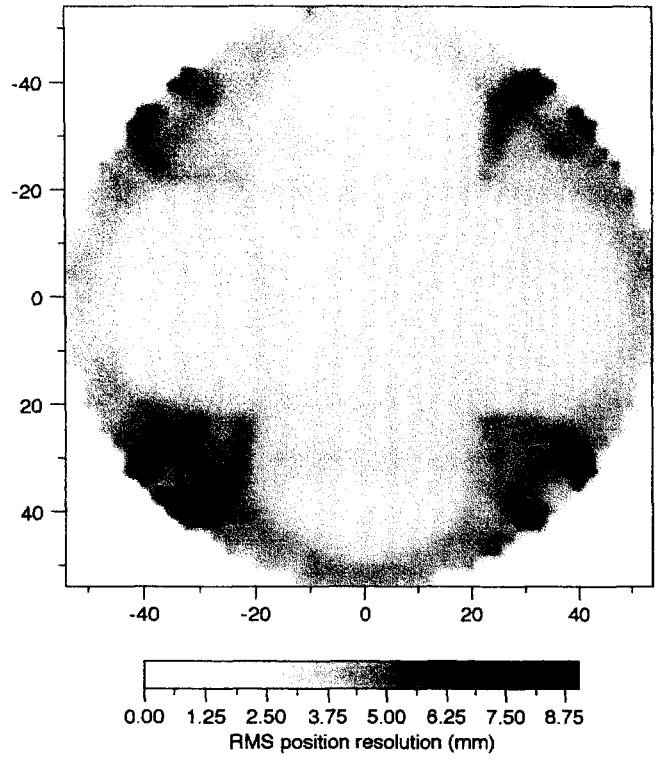


Figure 8. Derived position resolution on the tube face. Result of RMS combination of x and y one sigma fit widths of replayed calibration data. The region pattern can be seen in the image. The overall average resolution is 2.5 mm in each dimension (3.5 combined).

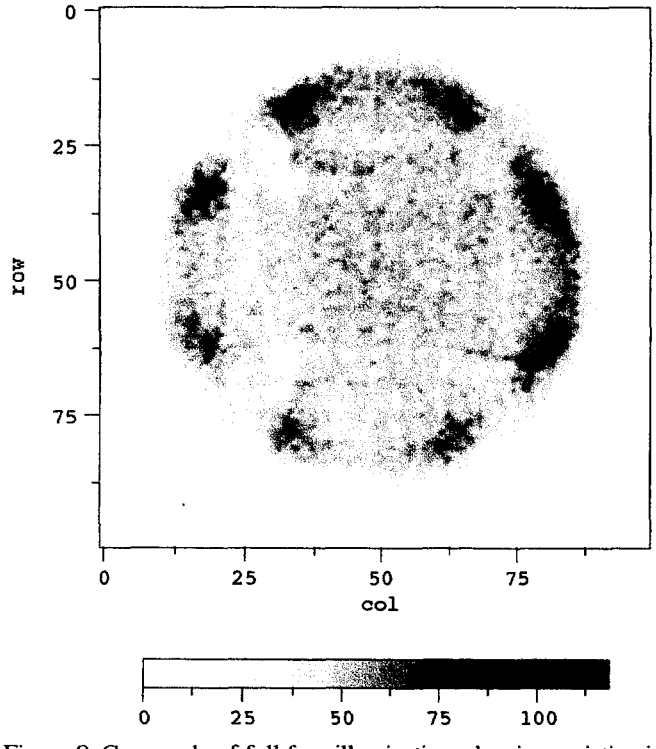


Figure 9. Grey scale of full face illumination, showing variation in Quantum efficiency. The bulk of the problems lie outside the area used for the coded aperture. However, residual evidence of the region structure can be seen.

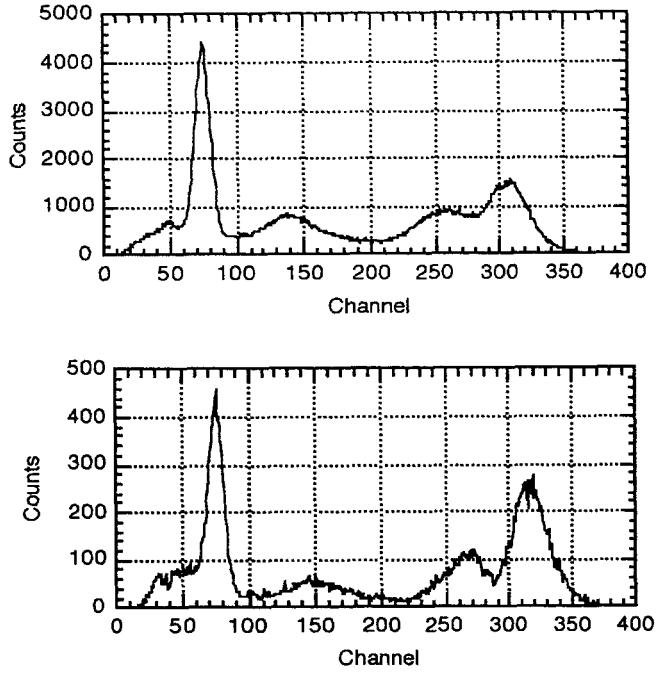


Figure 10. Energy spectrum from the $^{133}$Ba full face illumination data shown in Figure 9 (top) and from a single point at the tube center (bottom). The improved resolution at the single point is clearly evident in the separation of the higher energy peaks.

center of the tube. Although the full face performance is clearly inferior to that of the single point, a number of mitigating factors indicate that this can be improved. Of particular concern was a poor design to the high voltage circuit used during the scan (and subsequently replaced) which allowed the high voltage value to drift. This directly impacts the value of the energy calibration used in the linearization algorithm.

### *B. Electronics Design*

A simplified schematic of a single analog electronics channel, together with the control and logic circuitry is shown in Fig. 11. A total of eight analog channels are used in the full system. Each of the analog channels comprises a preamplifier, a buffer amplifier and a gated integrator. No shaping other than the integration period is used. The gated integrator outputs are passed to a sample and hold which maintains the output for the 80 $\mu$sec required for the Keitheley (KPCMCIA-16AI)[13] PCM/CIA ADC card to serially digitize the 8 channels. A leading edge discriminator applied to the last-dynode output is used to trigger the system. This has the advantage that the last dynode output represents a sum signal of all 8 anode outputs. For good energy resolution, we found a minimum value of order 7 $\mu$sec integration time was required. Given the long overall digitization time, we selected a 14 $\mu$sec integration width for the data presented here. During the acquisition time, subsequent events are not allowed to retrigger the system.

To fully accommodate the requisite dynamic range of the data, 12 bits are required. This seemingly large value for an alkali-halide based detector arises because both the energy and position information must be accommodated. In addition, one bit is required just to handle the factor of two variation in gain across the detector face. Although the digitizer provides 16 bits of data, in reality, the relatively poor performance in differential non-linearity, means only 12 bits can be used.

## IV. SOFTWARE

The imager software is based on a modified version of the code provided with RMD Corporation's RadCam imager. This system provides a graphical user interface to control acquisition, allowing for a number of advanced features as well as simple push-button operation. The code displays a video image scaled to the gamma-ray field of view on which a false-color gamma-ray image is superimposed. The energy spectrum can also be displayed and both this and the gamma-ray image are updated during acquisition. Before the start of an acquisition cycle, the energy spectrum can be used to select up to four energy regions-of-interest. Different gamma-ray images are generated for each of these during the integration and can be selected singly or summed in any combination as the gamma-ray image in the display. Finally, an event-mode run file of the data can be streamed to disk. By replaying this data off-line, a more detailed analysis can be performed including changes in the energy windows used. Complete information on the normal features of the code can be obtained from RMD Corp.

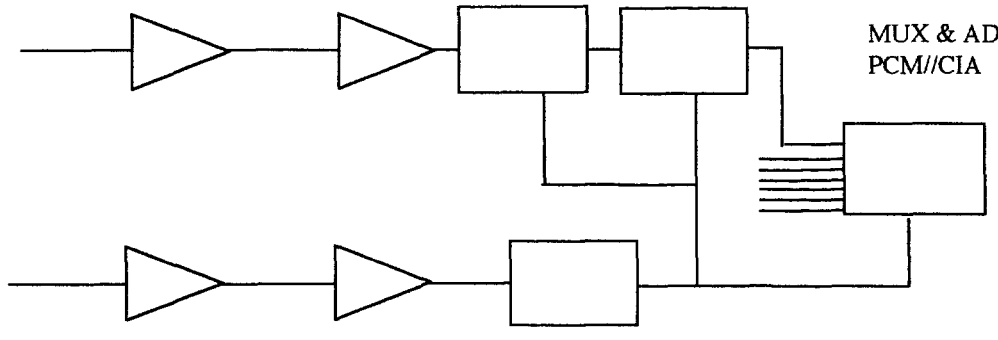


Figure 11. Electronics schematic. Each of the 8 analog channels is integrated and passed to a single digitizer via a long term sample and hold.

We have made a number of modifications to the RadCam software to allow operation with our imager. The event handling and

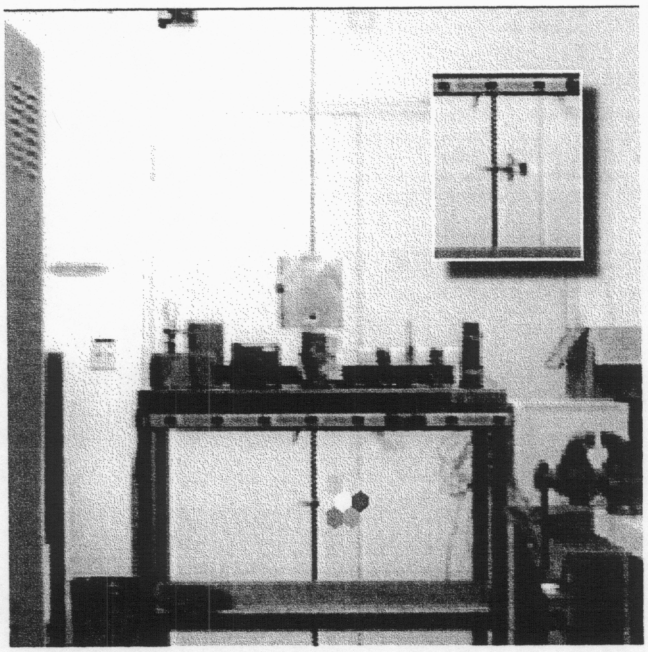

Figure 12. Composite gamma-ray/video image of a point source. On the computer screen, the video image is shown in black and white, and the gamma-ray image is shown in false-color based on the gamma-ray intensity. Gamma-ray pixels with less than a certain intensity (here 50%) can be turned off so the video iamge can be seen. The region behind the gamma-image has been inset in the top right of the Figure.

imaging routines were replaced to allow for our 8 channel acquisition system and modified linearization procedure. The image deconvolution routine was also modified to handle our HURA mask. Finally, the code was modified to allow for the 5 different zoom factors available on our imager. To provide for on-screen size information at the target, the user is prompted for an estimated distance to the sources before an acquisition is started. This is also required to correct for mask magnification by sources at finite distances.

## V. IMAGER PERFORMANCE

The overall performance of the system can be judged on the quality of the gamma-ray images obtained in a number of situations. The simplest application is to locate a single point source in the field of view. Typical performance in this application is shown in Fig. 12 where we imaged our collimated $^{133}$Ba source. The image of the 0.5 mCi source was taken in 4 mins at a distance of 5.5 m at an intermediate zoom factor of 2.4 the widest angle (Position resolution at the source is ~ 12 cm with the small hexes seen in the image 1/2 of that size.). This is actually one of a series of images taken as part of the video gamma alignment procedure, the last step in the imager calibration.

Of greater interest is the performance of the system with a complicated multi-source geometry. This is shown in Fig 13 where we image a cylinder of depleted uranium. As can be seen, within the ~ 5 cm position resolution of the image we obtain an accurate picture of the source distribution. The data was collected in 20 minutes at a distance of 230 cm at an intermediate zoom factor of 2.4.

## VI. FUTURE WORK

A number of improvements to the imager are in progress. One of our primary concerns is to replace the Keithley PCM/CIA card which performs the eight channel digitization using only a single ADC. This requires 80 $\mu$s for all eight channels, significantly impacting the system deadtime.

The linearization algorithm is also undergoing refinement. As can be seen in Fig. 9, there appear to be variations in the quantum efficiency as a function of position. The severity and shape of the variations has been found to depend on the order in which the sections are searched for an event location. Although we have used a search order which optimizes the uniformity it would be better to combine the data without an inherent ordering.

Preliminary work has been performed on a probability based region combination. In this approach, we define a probability to the position determination from each of the 9 regions and a weighted average of all the regions with acceptable data is used as the event location. The probability is generated based on the slope of the individual statistics in each dimension. The logic behind this approach is based on the direct correlation between the slope and the position resolution. The original results did not provide a significant improvement to the system position resolution although the quantum efficiency at the edges was improved.

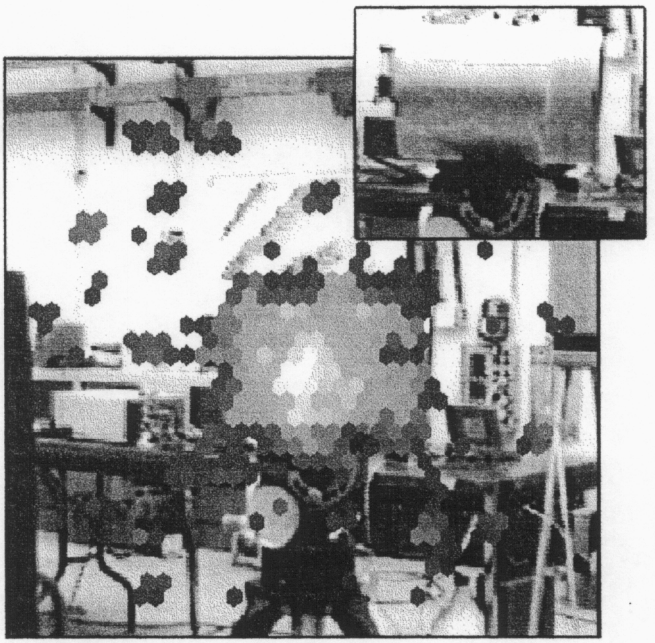

Figure 13. Image of a depleted uranium cylinder taken from 230 cm with a total of 20 min. integration time. The resolution element at the source is ~ 4 cm. The size of the hexagonal pixels visible in the image are ~ 2 cm. The cylinder is shown in the inset image at the top left of the figure.with the imager at a source resolution of 4 cm.

## VII. CONCLUSIONS

Gamma-ray imagers have demonstrated their utility in a number of terrestrial applications. This imager provides a new level of performance in gamma-ray imaging instrumentation. The new large area detector, coupled with the increased stopping power of a thicker scintillator crystal, significantly decreases the integration time required to obtain an image. This is accomplished without the complexity of trying to combine multiple images from different detectors. With the use of a mask which forms it's own anti-mask upon rotation and user-friendly software, out imager promises true "turn-key" operation for field use by non-experts.

## VIII. ACKNOWLEDGEMENTS

The authors gratefully acknowledge RMD corporation for providing the source code for their Radcam imager. James Wong at LLNL was instrumental in performing the code modifications. Tom Story and John Warhuse provided electronic design support and Paul McCandless mechanical design support.

## VIII. REFERENCES

1. F.E. Fenimore and T.M. Cannon, *Applied Optics*, **17**, 337 (1978).
2. K.P. Ziock, T.B. Gosnell, C.J. Hailey, J.H. Lupton, F.A. Harrison, *IEEE Trans. Nucl. Sci.* **39**, 1046 (1992)
3. *Development of a Measurement System for Imaging Deposits in Uranium Process Equipment*, K.P. Ziock, L. Madison, B.R. McGinnis, R.R. Royce and Angela Brown, Proceedings of the 36th Annual INMM meeting Palm Desert Ca., July 9-12, 1995.; *Transparency Measurements Using A Gamma-Ray Imager*, K.P. Ziock, L. Madison, Proceedings of the 36th Annual INMM meeting Palm Desert Ca., July 9-12, 1995.
4. RadCam by Radiation Monitoring Devices, 44 Hunt Street Watertown MA; GammaCam by AIL Systems Inc., 455 Commack Road Deer Park NY
5. D. L. Windt , F. E. Christensen, W. W. Craig, C. Hailey, F. A. Harrison, M. Jimenez-Garate, R. Kalyanaraman, and P. H. Mao, J. Appl. Phys., in press (2000).
6. E.E. Fenimore, *Applied Optics*, **17**, 3562 (1978).
7. W. R. Cook, M. Finger, T.A. Prince, E.C. Stone, *IEEE Trans. Nucl. Sci.*, **NS-31**, 771 (1984).
8. Hamamatsu Photonics K.K., 314-5, Shimokanzo, Toyooka-village, Iwata-gun, Shizuoka-ken, 438-0193, Japan
9. Rexon Components, Inc., 24500 High Point Road, Cleveland, OH. 44122
10. L. Nakae, K.P. Ziock, *SPIE Conf.* **3768**, (SPIE, Bellingham, 1999) p. 173.
11. C.J. Hailey, F. Harrison, J.H. Lupton, K.P. Ziock, *Nucl. Inst. Meth.* **A276**, 340 (1989).
12. W. Press, S. Teukolsky, W Vetterling, B. Flannery, Numerical Recipes in C (Cambridge University Press, New York, 1995) 683.
13. Keithley Instruments, Inc. 28775 Aurora Road, Cleveland OH.